The Astrophysical Journal, 985:77 (13pp), 2025 May 20 https://doi.org/10.3847/1538-4357/adc729

Late-time Evolution and Instabilities of Tidal Disruption Disks

Anthony L. Piro and Brenna Mockler
The Observatories of the Carnegie Institution for Science, Pasadena, CA 91101, USA; piro@carnegiescience.edu
Received 2024 December 5; revised 2025 March 9; accepted 2025 March 28; published 2025 May 15

Abstract

Observations of tidal disruption events on timescales of years after the main flare show evidence of continued activity in the form of optical/UV emission, quasiperiodic eruptions, and delayed radio flares. Motivated by this, we explore the time evolution of these disks, using semi-analytic models to follow the changing disk properties and feeding rate to the central black hole. We find that thermal instabilities typically begin ∼100 days after the TDE, causing the disk to cycle between high and low accretion states for up to ∼10 yr. The high state is super-Eddington, which may be associated with outflows that eject $\sim 10^{-3}$–$10^{-1}\,M_\odot$ over ∼1–2 days, with a range of velocities ∼0.03–0.3c. Collisions between these mass ejections may cause radio flares. In the low state, the accretion rate slowly grows over months to years, as continued fallback accretion builds the disk's mass. In this phase, the disk has a luminosity of $\sim 10^{41}$–10^{42} erg s^{-1} in the optical/UV, as seen in some late-time observations. Although the accretion cycles we find occur for a typical α-disk, in nature, the disk could be stabilized by other effects, such as the disk's magnetic field or heating from fallback accretion, the latter of which we explore. Thus, higher-cadence optical/UV observations along with joint radio monitoring will be key for following the disk state and testing these models.

Unified Astronomy Thesaurus concepts: Accretion (14); Transient sources (1851); Tidal disruption (1696); Supermassive black holes (1663)

1. Introduction

Tidal disruption events (TDEs) occur when an unfortunate star wanders too close to a supermassive black hole (BH), producing a spectacular electromagnetic transient (M. J. Rees 1988; E. S. Phinney 1989). For a TDE to be observable, the tidal disruption radius R_t must be exterior to the BH's gravitational radius (e.g., M. MacLeod et al. 2012). Otherwise, the star will be swallowed by the BH before it has a chance to be ripped apart. This puts a limit on the TDE-producing BH mass of $M_{\rm BH} \lesssim 10^8\,M_\odot$, which means TDEs are well suited for probing BHs and their environments in a mass range that is not usually observed in other supermassive BH studies (e.g., active galactic nuclei). Initial samples of TDEs are already providing mass estimates for BHs in the range of 10^6–$10^8\,M_\odot$ (e.g., B. Mockler et al. 2019) and, soon, with the Vera Rubin Observatory, the ability to study BH demographics in this way is going to increase exponentially (K. Bricman & A. Gomboc 2020).

A TDE is seen as a flare that lasts for many weeks to months and can be observed across a wide range of electromagnetic wavelengths (often for the same event). In recent years, it has become clear that TDE BHs can remain active for many years following the initial flare. One way this is seen is from the optical/UV emission that can persist from the TDE location (S. van Velzen et al. 2019; A. Mummery & S. A. Balbus 2020; M. Nicholl et al. 2024). Another is the presence of X-ray flares called quasiperiodic eruptions (QPEs; G. Miniutti et al. 2019, 2023b; M. Giustini et al. 2020; R. Arcodia et al. 2021, 2022, 2024; J. Chakraborty et al. 2021). It was expected that there was a connection between TDEs and QPEs due to host galaxy similarities (T. Wevers et al. 2022), theoretical arguments (A. Franchini et al. 2023; I. Linial & B. D. Metzger 2023), and persistent X-ray emission (J. Chakraborty et al. 2021; G. Miniutti et al. 2023a; E. Quintin et al. 2023), and this was confirmed by an optical TDE that years later produced QPEs (M. Nicholl et al. 2024).

This emission observed years after TDEs is generally thought to require a long-lasting disk. This would naturally produce the persistent optical/UV emission, and in the case of QPEs, a disk would be needed for either the star–disk collision models (e.g., A. Franchini et al. 2023; I. Linial & B. D. Metzger 2023) or the disk instability models (e.g., X. Pan et al. 2022; K. Kaur et al. 2023). R.-F. Shen & C. D. Matzner (2014) considered the viscous evolution of TDE accretion disks on a timescale of up to $\sim 10^4$ yr. They generally found that after a few months to about a year, a thermal instability would transition the disk to a gas-pressure-dominated low accretion state. This might naturally explain the jet shutoff at ∼500 days from the jetted TDE candidate Swift J1644+57 (A. J. Levan et al. 2011; B. A. Zauderer et al. 2013), but it makes the late-time optical/UV emission difficult to reconcile with the low expected accretion rate at these times. Nevertheless, groups have fit the late-time optical/UV and constructed disk models for the QPEs either by treating the disk scale height as a free parameter (e.g., A. Mummery et al. 2024) or by using an alternative viscosity prescription (e.g., S. van Velzen et al. 2019; which we discuss in more detail below). W. Lu (2022) updated the models from R.-F. Shen & C. D. Matzner (2014) by implementing a more detailed opacity treatment and a higher viscosity. I. Linial & B. D. Metzger (2024) also considered the evolution of TDE disks over long timescales but focused on potential feeding from the ablation of the QPE-producing star.

Many TDEs have also been seen to exhibit radio flares ∼100–3000 days after the main optical/UV emission (K. D. Alexander et al. 2020; A. Horesh et al. 2021a, 2021b; Y. Cendes et al. 2022; A. J. Goodwin et al. 2023a, 2023b;

C. T. Christy et al. 2024). As surveys have become more extensive, it seems this may be a common feature (A. Anumarlapudi et al. 2024; Y. Cendes et al. 2024). High-speed outflows or jet interactions with the circumnuclear medium at early times could produce radio emission via synchrotron radiation (e.g., R. A. Chevalier 1998; R. Barniol Duran et al. 2013; K. D. Alexander et al. 2016), but this has difficulty explaining the radio flares that occur with especially long delays of $\gtrsim$100 days. Some possible explanations include misaligned precessing jets (O. Teboul & B. D. Metzger 2023; W. Lu et al. 2024), a decelerated off-axis jet (T. Matsumoto & T. Piran 2024; I. Sfaradi et al. 2024), or outflow–cloud interactions (G. Mou et al. 2022; J. Zhuang et al. 2025). An interesting clue may be that the presence of these flares can be related to changes in the accretion state (e.g., I. Sfaradi et al. 2022), which again suggests that the late-time evolution of TDE disks is important.

The r- and g-band light curves years after TDEs show variations as well (A. Mummery et al. 2024). These are of higher cadence than the UV data, which makes them more sensitive to detecting these changes, and they generally show variations by a factor of $\sim$3. Some events exhibit even larger variations—for example, AT2021mhg and AT2020riz show an increase by a factor of $\sim$10, while AT2018lni shows variations in the g band by a factor of $\sim$6. This all points to the late-time emission not being as constant as may have been previously believed.

Motivated by these issues, we conduct a semi-analytic exploration of TDE accretion disks. In Section 2, we summarize the one-zone model we use in this work. This includes spelling out the guiding equations that are used to solve for the time evolution of the disk. We also explore the impact of a more detailed treatment of the opacity, comparing pure electron scattering to the Kramers and OPAL opacities (C. A. Iglesias & F. J. Rogers 1996). We show that our disk models cycle between low and high accretion states, and we discuss the physics that determines this and whether additional heating sources may stifle this instability. In Section 3, we compare our calculations to the work of R.-F. Shen & C. D. Matzner (2014). This is done to confirm the numerical methods we employ (which are discussed in more detail in the Appendix) and also to highlight the changes to the evolution we find due to differences in the treatment of the physics. We show that the higher opacities and viscosities we use are key to finding the accretion cycles that were not highlighted before (similar to the conclusions of W. Lu 2022).

We continue in Section 4 by summarizing the variety of disk evolutions we expect as a function of different TDE parameters. This shows that the accretion cycles happen more quickly for lower-mass BHs. The high accretion states are super-Eddington and may eject $\sim 10^{-3}$–$10^{-1}\,M_\odot$ on a timescale of $\sim$1–2 days. We compare our results to late-time observations in Section 5, showing that in the low accretion state, our models can match the $\sim 10^{42}\,\mathrm{erg\,s^{-1}}$ luminosities seen in the UV and $\sim 10^{41}\,\mathrm{erg\,s^{-1}}$ luminosities seen in the optical. Furthermore, we expect smaller variations in the optical bands than in higher-energy bands, and the factor of $\sim$3 variations we find roughly match observations. We conclude in Section 6 with a summary of our results and a discussion of future work.

2. One-zone Disk Model

To understand the evolution of an accretion disk left over from a TDE, we use a one-zone disk model (e.g., B. D. Metzger et al. 2008; R.-F. Shen & C. D. Matzner 2014; W. Lu 2022). Such a disk is characterized by a total mass M_d, a characteristic radius R_d (which is roughly the outer radius of the disk), and a disk angular momentum

$$J_d = (GM_{\rm BH}R_d)^{1/2}M_d, \tag{1}$$

where $M_{\rm BH}$ is the BH mass. Such a one-zone model can be a good approximation, since the majority of the disk mass and angular momentum are at R_d, the location that satisfies $t_\nu \sim t$, where t_ν is the viscous timescale. Since $t_\nu \sim r^{3/2}$, interior to R_d, the disk can be assumed to be in a steady state. In Section 6, we come back to this assumption and discuss whether a 1D model may be needed in some cases. We next explain the basic ingredients included to solve for the time-dependent disk properties.

2.1. Fallback Feeding During a TDE

When a star of mass M_* and radius R_* travels too close to a supermassive BH, it will be tidally disrupted if its pericenter distance R_p is smaller than the tidal disruption radius:

$$\begin{aligned} R_t &= R_*(M_{\rm BH}/M_*)^{1/3} \\ &= 7.0\times10^{12}M_6^{1/3}m_*^{-1/3}r_*\,\mathrm{cm}, \end{aligned} \tag{2}$$

where $M_{\rm BH}$ is the mass of the BH, $M_6 = M_{\rm BH}/10^6\,M_\odot$, $m_* = M_*/M_\odot$, and $r_* = R_*/R_\odot$. The depth of the star's plunge is usually described by the parameter $\beta = R_t/R_p$, so that $1 \lesssim \beta \lesssim R_t/R_s$, where $R_s = 2GM_{\rm BH}/c^2$ is the Schwarzschild radius (the last ratio can be larger for a Kerr BH). The critical value for a complete disruption β_c depends on the central concentration of the state (J. Guillochon & E. Ramirez-Ruiz 2013; J. A. P. Law-Smith et al. 2020; T. Ryu et al. 2020)—for example, $\beta_c = 1.85$ for an $n = 4/3$ polytrope and $\beta_c = 0.9$ for an $n = 5/3$ polytrope.

The fallback of stellar material can be modeled as a power law for times greater than $t_{\rm fb}$ (e.g., M. J. Rees 1988; E. S. Phinney 1989):

$$\dot{M}_{\rm fb}(t) = \frac{M_*}{5t_{\rm fb}}\left(\frac{t}{t_{\rm fb}}\right)^{-5/3}, \tag{3}$$

where the fallback timescale is (e.g., N. Stone et al. 2013)

$$\begin{aligned} t_{\rm fb} &= \frac{\pi R_t^3}{(2GM_{\rm BH}R_*^3)^{1/2}} \\ &= 3.5\times10^6M_6^{1/2}m_*^{-1}r_*^{3/2}\,\mathrm{s}. \end{aligned} \tag{4}$$

In this expression, we use R_t rather than R_p, because for full disruptions with $\beta > \beta_c$, the dependence is generally weaker with β than what would be expected from analytic arguments (J. Guillochon & E. Ramirez-Ruiz 2013; N. Stone et al. 2013; E. Gafton & S. Rosswog 2019). The peak fallback rate is then

$$\frac{M_*}{5t_{\rm fb}} = 1.8\,M_6^{-1/2}m_*^2r_*^{-3/2}\,M_\odot\,\mathrm{yr}^{-1}. \tag{5}$$

Although these scalings match numerical results for $t > t_{\rm fb}$, we also need the rising $\dot{M}_{\rm fb}(t)$ for the early phases of the disk

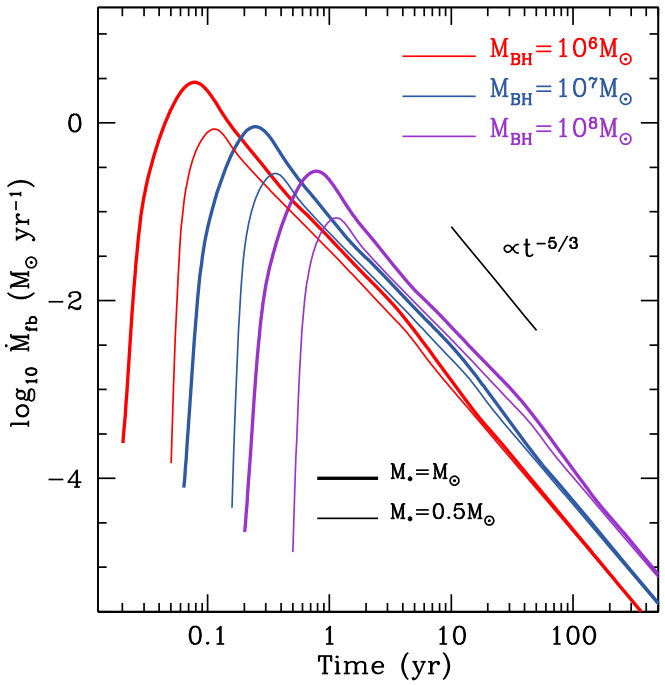

Figure 1. Fallback accretion rate for tidal disruptions of stars using the work of J. Guillochon & E. Ramirez-Ruiz (2013), for $M_* = M_\odot$ with $n = 4/3$ and $\beta = 1.85$ (thick lines) and $0.5\,M_\odot$ with $n = 5/3$ and $\beta = 0.9$ (thin lines). The three colors correspond to different values of $M_{\rm BH}$, as indicated.

evolution. Thus, we use the numerical results of J. Guillochon & E. Ramirez-Ruiz (2013) for our full calculations, which we present for three BH masses and two stellar masses in Figure 1. In each of these cases, we use $\beta = \beta_c$, since we are interested in full disruptions and $\dot{M}_{\rm fb}(t)$ does not change too greatly for $\beta \gtrsim \beta_c$. In most of this work, we generally use $\beta = \beta_c$, unless we state otherwise.

The fallback material circularizes at a radius

$$R_c = 2R_p = 1.4 \times 10^{13}\beta^{-1}M_6^{1/3}m_*^{-1/3}r_* \,{\rm cm}. \quad (6)$$

Thus, as the fallback material is incorporated into the accretion disk, it has the specific angular momentum

$$\begin{aligned} j_{\rm fb} &= (GM_{\rm BH}R_c)^{1/2} \\ &= 4.3 \times 10^{22}\beta^{-1/2}M_6^{2/3}m_*^{-1/6}r_*^{1/2} \,{\rm cm^2\,s^{-1}}. \end{aligned} \quad (7)$$

In detail, the fallback stream may interact at a different radius than R_c. For example, if the stream and disk are in a similar plane, then the collision may occur near the outer edge of the disk, at R_d. Nevertheless, the most important issue is the angular momentum contribution, so we use Equation (7) for this work.

2.2. Time Evolution Equations

The disk is fed via the fallback of material from the TDE at a rate $\dot{M}_{\rm fb}$, as described above, which then accretes through the disk at a rate $\dot{M}$. Some fraction of this mass transport may go into an outflow, while the remaining mass accretes all the way down to the BH. The outflow is expected to be launched within the spherization radius $R_{\rm sph}$, where the local accretion luminosity $GM_{\rm BH}\dot{M}/R_{\rm sph}$ exceeds the the Eddington luminosity $4\pi GM_{\rm BH}c/\kappa$ (M. C. Begelman 1979):

$$R_{\rm sph} = \min\left(R_d, \frac{\kappa\dot{M}}{4\pi c}\right), \quad (8)$$

where we use an electron-scattering opacity for κ. Following previous studies (e.g., B. D. Metzger et al. 2008; F. Yuan & R. Narayan 2014; H. Hu et al. 2022), we assume these disk outflows cause the mass inflow rate to decrease within $R_{\rm sph}$ as it approaches the BH (e.g., R. D. Blandford & M. C. Begelman 1999):

$$\dot{M}(r) = \left(\frac{r}{R_{\rm sph}}\right)^p \dot{M}, \quad (9)$$

where $0 < p < 1$ is a parameter that controls the strength of the outflow. The total mass outflow rate is thus

$$\dot{M}_{\rm out} = \left[1 - \left(\frac{R_i}{R_{\rm sph}}\right)^p\right]\dot{M}, \quad (10)$$

where R_i is the inner radius of the disk. Even with an outflow, the total mass loss of the disk at any time adds up to $\dot{M}$, and thus the differential equation

$$\frac{dM_d}{dt} = \dot{M}_{\rm fb} - \dot{M} \quad (11)$$

describes the mass evolution. This expression assumes that the mass feeding rate to the disk tracks the fallback rate. If stream collisions are responsible for circularizing material into a disk to begin with (as opposed to, e.g., nozzle shocks; see E. Steinberg & N. C. Stone 2024), Lense–Thirring precession by a rapidly spinning BH can delay this process, by causing the stream to miss colliding with itself for many orbits (L. Dai et al. 2013; J. Guillochon & E. Ramirez-Ruiz 2015; T. Jankovifç et al. 2024). The details of this depend on the general relativistic precession versus the hydrodynamic evolution of the stream thickness. The circularization process still needs further exploration, so by simply using $\dot{M}_{\rm fb}$, our results are focused on the period after material has begun to circularize into a disk.

We next consider the disk's angular momentum evolution. Fallback adds angular momentum with a specific value of $j_{\rm fb}$, but it can also be removed via the outflows. These two processes are represented in the following differential equation:

$$\frac{dJ_d}{dt} = j_{\rm fb}\dot{M}_{\rm fb} - C(GM_{\rm BH}R_{\rm sph})^{1/2}\dot{M}_{\rm out}, \quad (12)$$

where the constant C is determined by the torque exerted by the wind on the disk. Assuming that the outflow produces no net torque (e.g., J. M. Stone & J. E. Pringle 2001), then the angular momentum losses are due to the specific angular momentum at each disk radius, resulting in

$$C = \frac{2p}{2p+1} \quad (13)$$

(P. Kumar et al. 2008). In principle, this factor can be higher if large-scale magnetic fields help transport additional angular momentum loss, but we do not consider these effects in this work.

2.3. Disk Structure

The mass-loss rate $\dot{M}$ is set using a typical vertically integrated disk model. We quickly summarize the model here for completeness (mostly following J. Frank et al. 2002).

Hydrostatic balance gives a disk thickness of $H = c_s/\Omega$, where $c_s^2 = P/\rho$ is the isothermal sound speed, P and ρ are the midplane pressure and density, respectively, and $\Omega = (GM_{\rm BH}/R_d^3)^{1/2}$ is the Keplerian angular speed. For the pressure, we include both ideal gas and radiation components, so that

$$P = P_g + P_r = \frac{\rho k_{\rm B} T}{\mu m_p} + \frac{aT^4}{3}, \tag{14}$$

where $k_{\rm B}$ is Boltzmann's constant, μ is the mean molecular weight (0.62 for solar material), m_p is the proton mass, and a is the radiation constant.

The surface density is $\Sigma = \rho H$, and mass conservation through the disk leads to $\dot{M} = 3\pi\nu\Sigma$, where ν is the viscosity. We parameterize the viscosity using the usual α-disk model (N. I. Shakura & R. A. Sunyaev 1973):

$$\nu = \alpha c_s H = \alpha \frac{P}{\Omega\rho}, \tag{15}$$

where α is constant with a typical value of $\alpha = 0.1$. It has long been known that simple 1D theory results in disks that are viscously and thermally unstable when the disk is radiation-pressure-dominated and cooled radiatively (A. P. Lightman & D. M. Eardley 1974; N. I. Shakura & R. A. Sunyaev 1976). This can be alleviated by setting P to P_g in Equation (15), as in P. J. Sakimoto & F. V. Coroniti (1981), and, in fact, such a prescription is employed by S. van Velzen et al. (2019) when fitting late-time UV emission from TDEs. Whether these instabilities exist for more realistic magnetohydrodynamic simulations of accretion disks in 3D is still not clear (e.g., M. C. Begelman & J. E. Pringle 2007; S. Hirose et al. 2009; H. Oda et al. 2009; Y.-F. Jiang et al. 2013; B. Mishra et al. 2016; A. Sadowski 2016), and this may even depend on the details of the radiative transfer and opacity (Y. F. Jiang et al. 2016). Here, we focus on the more classical case given by Equation (15) using the total pressure, and we explore the implications if these instabilities really do occur in nature.

The internal energy in the disk is determined by viscous heating $Q^+ = 9\nu\Sigma\Omega^2/8$, radiative cooling $Q_{\rm rad}^- = acT^4/(3\kappa\Sigma)$, where κ is the specific opacity, and advective cooling:

$$Q_{\rm adv}^- = \frac{\dot{M}}{2\pi R_d^2} c_s^2 \xi, \tag{16}$$

where ξ is the logarithmic entropy gradient. Since ξ is typically of order unity, we set $\xi = 1.5$ for this work (e.g., K.-y. Watarai 2006). The local energy balance results in

$$\frac{9}{8}\nu\Sigma\Omega^2 = \frac{acT^4}{3\kappa\Sigma} + \frac{\dot{M}}{2\pi R_d^2} c_s^2 \xi. \tag{17}$$

We ignore energy lost to the wind, although see the Appendix of R.-F. Shen & C. D. Matzner (2014) for a discussion of the small correction from this effect. We also do not include energy loss from vertical convection, which may be particularly important when the disk is super-Eddington (Y.-F. Jiang et al. 2013).

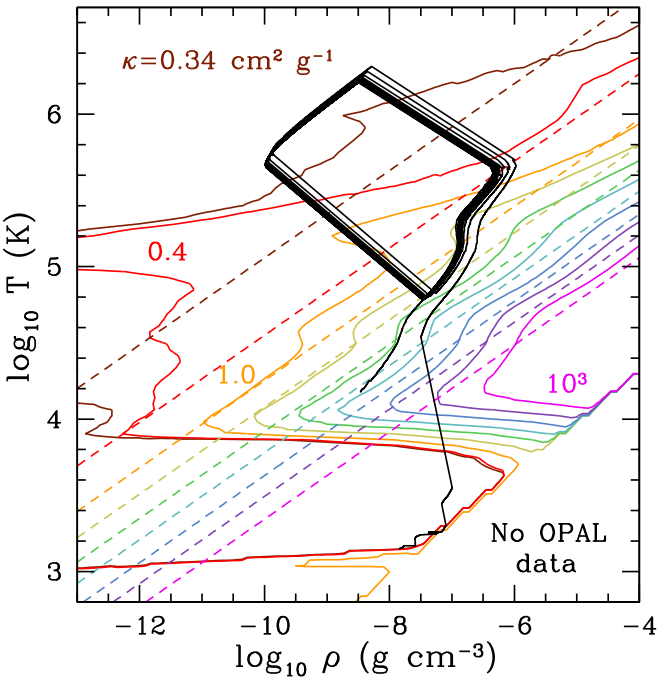

Figure 2. Contours of constant opacity for solar composition material from OPAL (solid colored lines) in comparison to an analytic Kramers-plus-electron-scattering opacity given by Equation (18) (dashed colored lines). The dark red and red curves are contours of constant opacity, with values of $0.34\,{\rm cm^2\,g^{-1}}$ and $0.4\,{\rm cm^2\,g^{-1}}$, respectively. The orange through magenta curves are spaced logarithmically in intervals of $10^{0.5}$, from $1.0\,{\rm cm^2\,g^{-1}}$ to $10^3\,{\rm cm^2\,g^{-1}}$. The black solid line shows the trajectory of a fiducial disk solution ($M_{\rm BH} = 10^6\,M_\odot$, $M_* = M_\odot$, $\beta = 1.85$, and $\alpha = 0.1$) evolved over 5 000 yr.

An important issue when solving Equation (17) is setting κ in $Q_{\rm rad}^-$. In previous works addressing similar problems related to the long-term evolution of TDE disks, this has been set to purely electron scattering $\kappa = \kappa_{\rm es} = 0.34\,{\rm cm^2\,g^{-1}}$ (e.g., R.-F. Shen & C. D. Matzner 2014) or a sum of electron scattering and Kramers opacities (e.g., I. Linial & B. D. Metzger 2024):

$$\kappa = \kappa_{\rm es} + \kappa_0 \rho T^{-7/2}, \tag{18}$$

where ρ and T are assumed to be in cgs units and $\kappa_0 = 5 \times 10^{24}\,{\rm cgs}$. In Figure 2, we plot contours of the constant κ using Equation (18) as dashed colored lines, in comparison to the Rosseland mean opacities from OPAL (C. A. Iglesias & F. J. Rogers 1996) for solar composition material as solid colored lines. Some important features that are seen for the OPAL opacities that are not captured in a simpler analytic opacity include the following:

1. An enhanced opacity near $T \approx 2 \times 10^5\,{\rm K}$ due to the iron opacity "bump" (as explored by Y. F. Jiang et al. 2016).
2. A strong decrease in opacity for $T \lesssim 6 \times 10^3\,{\rm K}$, due to hydrogen recombination.
3. A slightly enhanced opacity in the range of $\approx 4 \times 10^4$–$5 \times 10^5\,{\rm K}$, which as we will show is especially relevant for the accretion disks we will be considering.

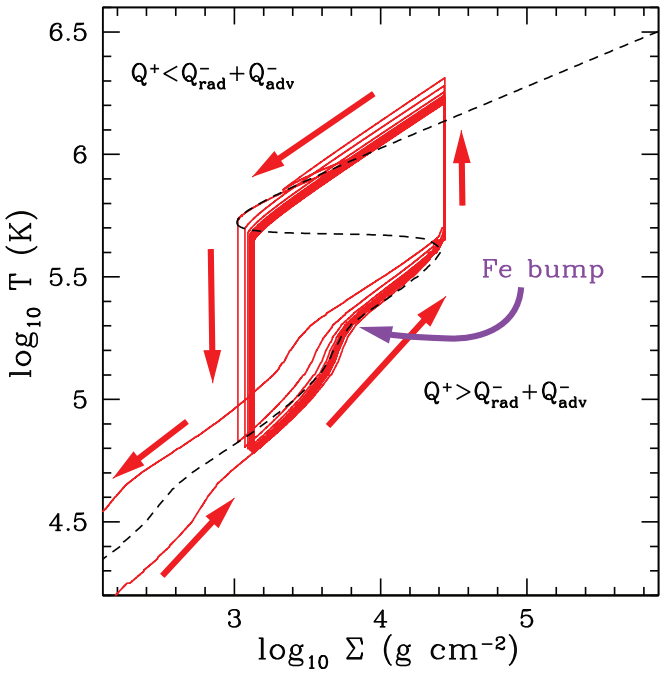

Figure 3. The black dashed line represents the surface density Σ and temperature T for equilibrium disk solutions, using $M_{\rm BH} = 10^6\,M_\odot$, $\alpha = 0.1$, a fixed radius of $R_d = 3 \times 10^{13}$ cm, and varying $\dot{M}$ from high to low values, going from top to bottom. Cooling beats heating on the left of these solutions, and heating beats cooling on the right. The red solid line shows an example disk evolution. The disk starts from the bottom left corner and evolves toward the right. Once it reaches the instability region, the disk cycles counterclockwise in this space, alternating between low and high states. In purple, we highlight where the iron opacity bump impacts the evolution.

Also plotted on Figure 2 as a solid black line is an example disk evolution. We will come back to the details of this later (the methods for how this is solved for are described in the following sections) but include it now to highlight the regions of temperature and density space that will be most relevant to this study. In particular, one can directly see the imprint of the the iron bump on the right side of the trajectory.

The example disk evolution in Figure 2 circles around in density and temperature, due to a thermal instability. Since this plays an important role in our results and future discussions, we focus more on this instability in Figure 3. We calculate a series of equilibrium disk solutions by solving Equation (17) for a range of $\dot{M}$, using $M_{\rm BH} = 10^6\,M_\odot$ and $\alpha = 0.1$. We fix the disk radius to $R_d = 3 \times 10^{13}$ cm. This results in a locus of solutions, shown as a dashed line in Figure 3. To the left of the dashed line, cooling exceeds heating, and to the right of the dashed line, heating beats cooling. Even though all of the points on this dashed line are equilibrium solutions, it is well known that regions where $dT/d\Sigma < 0$ are thermally unstable (A. P. Lightman & D. M. Eardley 1974; N. I. Shakura & R. A. Sunyaev 1976). This is in the regime where the disk is radiation-dominated, i.e., $P_{\rm rad} > P_{\rm gas}$, and radiatively cooled, i.e., $Q^-_{\rm rad} > Q^-_{\rm adv}$. In fact, when we extend these models to even lower accretion rates and cooler temperatures ($\lesssim 6 \times 10^3$ K), another "S curve" occurs, due to the abrupt change in opacity from hydrogen recombination. This physics is of course important for dwarf nova outbursts (B. Warner 1995) but would only be exhibited at extremely late times by TDEs and is thus outside the scope of this work.

This instability is exhibited by the example time-dependent evolution we show in red (this is the same example model as plotted in Figure 2). This model starts at low Σ and T at the bottom left corner of the plot and then evolves toward the top right as the disk mass builds. It then goes through cycling behavior when it reaches the unstable region. After circling counterclockwise many times, eventually, once $\dot{M}_{\rm fb}$ is sufficiently low, the disk continues to evolve in the low state toward the bottom left corner. Note that the black and red lines do not coincide exactly, because in the time-dependent model, R_d is allowed to vary, while for the equilibrium solutions, R_d is fixed. Nevertheless, the equilibrium solution roughly predicts where the instability arises. Finally, we again highlight the impact of the iron opacity bump (which occurs where the purple arrow points). This essentially creates a two-tiered low state, which is an important property of the time evolution we will come back to later.

2.4. Fallback Heating

A potentially important physical effect that we do not include in our main models is the interaction of the fallback accretion with the spreading accretion disk. This collision can add additional heating to the disk and modify the energy balance given by Equation (17). How well the fallback stream is thermalized depends on the ram pressure of the incoming material, the pressure in the disk, and the trajectory of the fallback, which is related to the hydrodynamics and dynamics of the stream and disk, so we save a detailed treatment of this for future work. Nevertheless, the heating rate should be proportional to $\dot{M}_{\rm fb} v_{\rm fb}^2/2$, where $v_{\rm fb} \approx (GM_{\rm BH}/R_d)^{1/2}$. Note that a similar prescription for this heating was used by W. Lu (2022). We use R_d rather than R_c for setting this velocity, which assumes that the incoming stream is in a similar plane to the disk and thus will collide somewhere near the outer radius of the disk. Using this, we estimate the impact of including such effects, by rewriting the energy equation as

$$\frac{9}{8}\nu\Sigma\Omega^2 + \frac{\eta\dot{M}_{\rm fb}}{4\pi R_d^2}v_{\rm fb}^2 = \frac{acT^4}{3\kappa\Sigma} + \frac{\dot{M}}{2\pi R_d^2}c_s^2\xi, \tag{19}$$

where $\eta \lesssim 1$ is a parameter that sets the efficiency of the thermalization. Implicit in this equation is the assumption that the heat will spread fairly quickly around the disk, even though the stream collision occurs at a single point.

In Figure 4, we recalculate the equilibrium solutions from Figure 3 but now including fallback heating, using the updated energy Equation (19) with $\eta = 1$ and varying the value of $\dot{M}_{\rm fb}$. This shows that when $\dot{M}_{\rm fb} = M_\odot\ {\rm yr}^{-1}$, for this particular example, the instability no longer occurs. As we decrease $\dot{M}_{\rm fb}$, the instability reappears, and at $\dot{M}_{\rm fb} = 10^{-6}\,M_\odot\ {\rm yr}^{-1}$, the equilibrium solutions are basically the same as not including fallback heating at all (the black dashed line).

Note that for this treatment, η and $\dot{M}_{\rm fb}$ are degenerate with one another, so the exact fallback value where the instability disappears depends on η. We conducted a series of time evolution calculations with different levels of heating (not presented in this work) and found that for high η, the instability can be removed at early times, which causes $\dot{M} \approx \dot{M}_{\rm fb}$. This is similar to the results of I. Linial & B. D. Metzger (2024), who also found that the disk can be stabilized with an additional heating source, but in their case, this was from the shock by the QPE-generating star colliding with the disk.

C. Bonnerot et al. (2021) studied stream interactions and found that most of the orbital energy is dissipated by shocks

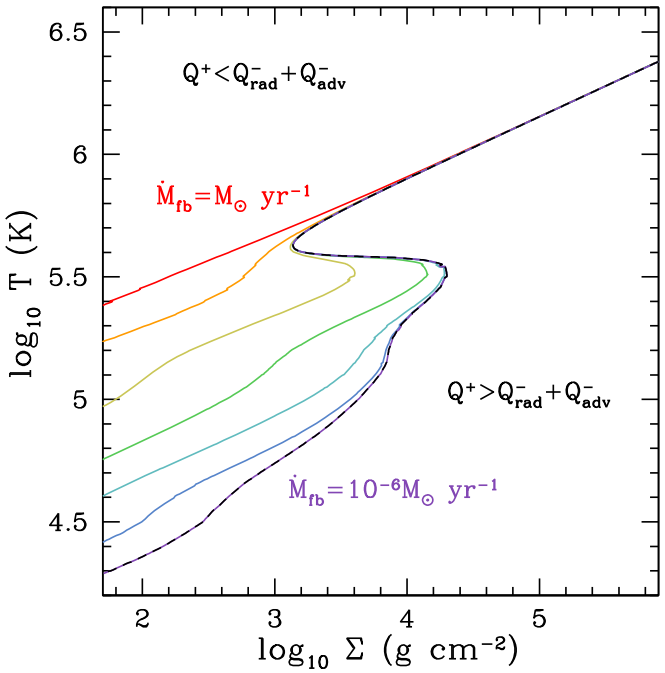

Figure 4. The black dashed line matches the same line from Figure 3. The solid colored lines show the new equilibrium solutions when heating from fallback accretion is included using Equation (19) (all using $\eta = 1$, $M_{\rm BH} = 10^6\,M_\odot$, $\alpha = 0.1$, a fixed radius of $R_d = 3 \times 10^{13}$ cm, and varying $\dot{M}$ from high to low values, going from top to bottom). The different colors correspond to varying the fallback accretion by factors of 10 from $\dot{M}_{\rm fb} = M_\odot\ {\rm yr}^{-1}$ (red line) to $\dot{M}_{\rm fb} = 10^{-6}\,M_\odot\ {\rm yr}^{-1}$ (purple line). Note that the black dashed and purple lines are basically coincident.

that are away from the disk if there is a strong stream self-crossing shock that diverts the fallback in a somewhat spherical manner. This suggests that $\eta \ll 1$, which would make disk stabilization from fallback difficult. This is not a solved problem, though, and these uncertainties show that future work is needed to better understand the interactions between the fallback gas and an existing disk, so that the amount of heating can be better assessed.

3. Comparisons to Previous Work

To find the disk evolution, we solve the differential Equations (11) and (12) explicitly, where $\dot{M}$ is set using the energy balance as given by Equation (17) and described in Section 2.3. In the Appendix, we describe the numerical scheme used to solve for the disk structure and time evolution. To check our approach, in this section, we make comparisons in some simplified limits.

To facilitate comparisons to R.-F. Shen & C. D. Matzner (2014), we had to update some of the prescriptions we use in our disk model (our work is set to be consistent with J. Frank et al. 2002). To quickly summarize the differences, these are $\Sigma = 2\rho H$, $\nu = 2\alpha c_s H/3$, $Q^+ = 9\nu\Sigma\Omega^2/4$, $Q^-_{\rm rad} = 4acT^4/(3\kappa\Sigma)$, and setting $\xi = 1$. We also assume here that all accretion above the Eddington rate is ejected, rather than using the radially varying mass-loss rate as described by Equation (10). We use these values and relations for the remainder of this section, but for all other calculations shown in this work, we use the prescriptions summarized in Section 2.

In addition, R.-F. Shen & C. D. Matzner (2014) use the analytic fallback rate given in Equation (3) rather than the numerical fallback rates we show in Figure 1. Integrating Equation (3) from $t = t_{\rm fb}$ to $t = \infty$ results in a mass of $3\,M_*/10$. They assume that an additional mass of $M_*/5$ circularizes during the time $\sim t_{\rm fb}$, so that basically $\sim t_{\rm fb} \times \dot{M}_{\rm fb}(t_{\rm fb})$ sets the initial mass of the disk. This then sums to give a total fallback mass of $M_*/2$, as is well known.

We compare our calculations to the work of R.-F. Shen & C. D. Matzner (2014) in Figure 5. We scale the disk radius to R_c and the accretion rate to the Eddington rate,

$$\dot{M}_{\rm Edd} = L_{\rm Edd}/c^2 = \frac{4\pi G M_{\rm BH}}{\kappa_{\rm es} c} = 2.6 \times 10^{-2} M_6\,M_\odot\ {\rm yr}^{-1}, \quad (20)$$

where $L_{\rm Edd}$ is the Eddington luminosity, to mimic their Figure 7 as closely as possible. Their "fiducial model" (blue solid line) uses $M_{\rm BH} = 10^6\,M_\odot$, $M_* = M_\odot$, $\beta = 1$, $\alpha = 0.01$, and purely $\kappa = \kappa_{\rm es}$ for the opacity (see the upper left panel of their Figure 7). We get $R_d \propto t^{2/3}$ at early times, like R.-F. Shen & C. D. Matzner (2014). The accretion rate and radius then drop dramatically at $t \approx 10^{-0.6}$ yr, due to the thermal instability. The accretion rate slowly increases as the disk builds from fallback accretion. At late times, once $\dot{M}_{\rm fb} \ll \dot{M}$, the disk obeys the power-law behavior $\dot{M} \propto t^{-19/16}$ and $R_d \propto t^{3/8}$, as derived by J. K. Cannizzo et al. (1990).

The other models in Figure 5 explore what happens as we change the model parameters away from the fiducial values used by R.-F. Shen & C. D. Matzner (2014). First, we use the OPAL opacities, rather than strictly electron scattering (red dashed lines). The evolution is mostly the same, with the main differences being the late-time radius and an increased $\dot{M}$ during the low state. Next, we increase the viscosity to $\alpha = 0.1$ and use the analytic opacity from Equation (18) (green dotted–dashed lines). The higher viscosity makes the disk evolve more quickly, increasing the disk radius at early times and then causing the disk to go through multiple cycles of low and then high states for a few years, until $\dot{M}_{\rm fb} \lesssim \dot{M}$. We note that such cycles were also seen in a subset of the models explored by R.-F. Shen & C. D. Matzner (2014), although this was not the focus of their work. Finally, we use $\alpha = 0.1$ with the full OPAL opacities (purple dotted line). Although the high states now appear at different times, in comparison to the previous model, the evolution is qualitatively similar. An interesting detail is that with the OPAL opacities, $\dot{M}$ is slightly larger as it rises toward a high state.

To further explore the differences between these models, we plot them as a function of Σ and T in Figure 6. This helps us better focus on how the different models evolve through the thermal instability (as seen from Figure 3). Initially, all four models start with a similar Σ and T at the top right corner of the plot, then evolve toward the bottom left. (Unlike in Figure 3, these models start at high accretion rates, because of the large initial disk mass that is assumed.) The lower-α models (blue solid and red dashed lines) hit the instability at larger Σ and T (but not necessarily earlier in time, since the viscous time is also controlled by α), and quickly drop to the low state. They then climb to the right, due to continued feeding from fallback accretion, but they never gain quite enough mass to transition back to the high state and instead eventually trace back toward the left again. One can see that the increased OPAL opacities dramatically raise the position of the low state for these models.

The two high-α models (green dotted–dashed and purple dotted lines) evolve fairly similarly, with the high state

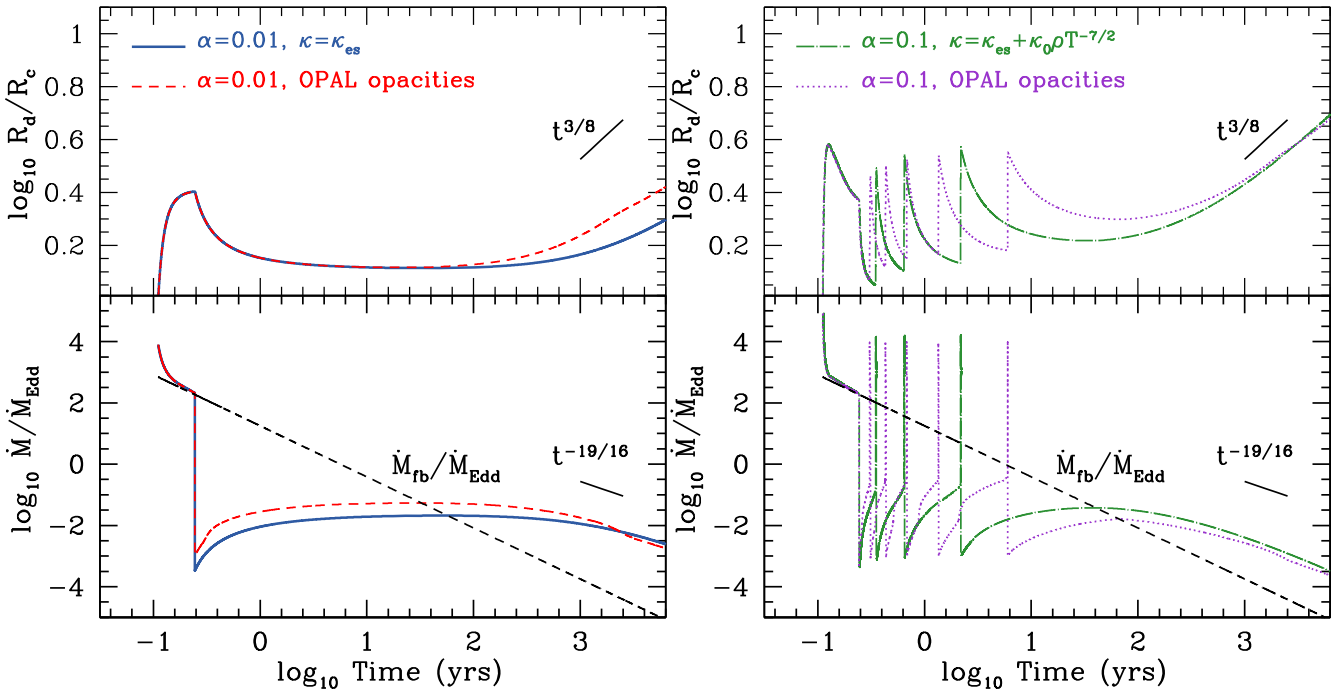

Figure 5. Comparison of the disk radius and accretion evolution for four different models. In each case, we use $M_{\rm BH} = 10^6\,M_\odot$, $M_* = M_\odot$, and $\beta = 1$ with the analytic fallback rate given in Equation (3). In the upper plot, we set $\alpha = 0.01$ and compare $\kappa = \kappa_{\rm es}$ (blue solid lines, meant to mimic the fiducial model from R.-F. Shen & C. D. Matzner 2014), with κ set by the OPAL opacities (red dashed lines). In the lower plot, we set $\alpha = 0.1$ and compare κ using an analytic opacity given by Equation (18) (green dotted–dashed lines) and $\alpha = 0.1$, with κ again set by the OPAL opacities (purple dotted lines). The late-time power-law behavior was derived in R.-F. Shen & C. D. Matzner (2014). The dashed black line indicates the fallback accretion rate that is feeding the disk.

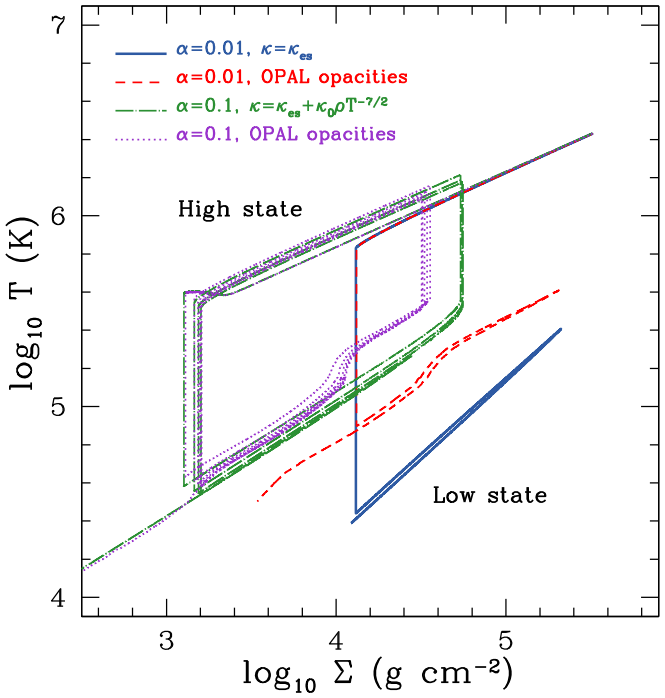

Figure 6. The same disk evolution solutions as shown in Figure 5 but instead plotted as a function of the surface density Σ and temperature T. This highlights how these solutions change between high and low accretion states as they evolve through the thermal instability.

extending to somewhat lower temperatures, before falling to the low state and then having an even hotter low state, due to the higher α value. The important difference here is due to the iron opacity bump, which increases the temperature and shortens the length of the low state.

4. Exploring the Disk Solutions

Now that we have confirmed our methods and explained the differences between our results and previous work, we return to the prescriptions described in Section 2, along with the numerical fallback rates presented in Figure 1. We calculate a suite of disk evolutions with time and summarize some of the main results here.

4.1. Dependence on BH Mass

In Figure 7, we consider three BH masses and focus on the first year of the evolution, to highlight the features present early on. It can be seen that during each outburst, the disk mass decreases dramatically, due to the increased $\dot{M}$. The disk radius correspondingly increases, to conserve angular momentum. Then, during the low state, the accretion rate grows as the mass of the disk builds from fallback accretion. The radius during the low state shrinks, because the fallback material has less specific angular momentum than the disk material. The BH mass plays an important role in setting the viscous time in the disk. For a larger $M_{\rm BH}$, the cycling between high and low states is much slower, the disk mass M_d is generally higher, and the disk radius R_d gets pushed to larger values.

The early evolution also changes for different $M_{\rm BH}$ values. For $M_{\rm BH} = 10^6\,M_\odot$, the disk accretion rate closely follows the fallback rate, while for $M_{\rm BH} = 10^7\,M_\odot$ or $10^8\,M_\odot$, the accretion rate is well below the fallback rate, except during the high states. The reason for this is that the fallback evolution is slow for high-mass BHs, so accretion prevents the disk from building at early times. Whether or not this happens for real TDEs likely depends on the details of the circularization process and when a viscous accretion disk is actually established. It may also depend on whether heating from the

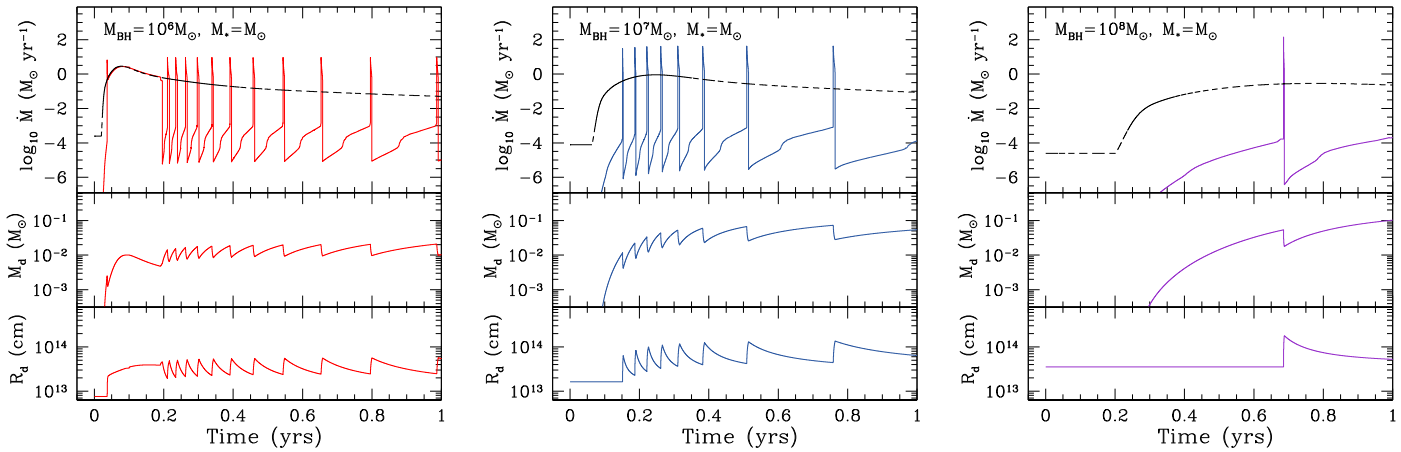

Figure 7. Evolution of the accretion rate $\dot{M}$, disk mass M_d, and disk radius R_d over the first year, using $M_* = M_\odot$, $\beta = 1.85$, $\alpha = 0.1$, and $p = 0.5$ for three different values of $M_{\rm BH}$, as indicated. The black lines delineate the fallback accretion rate $\dot{M}_{\rm fb}$.

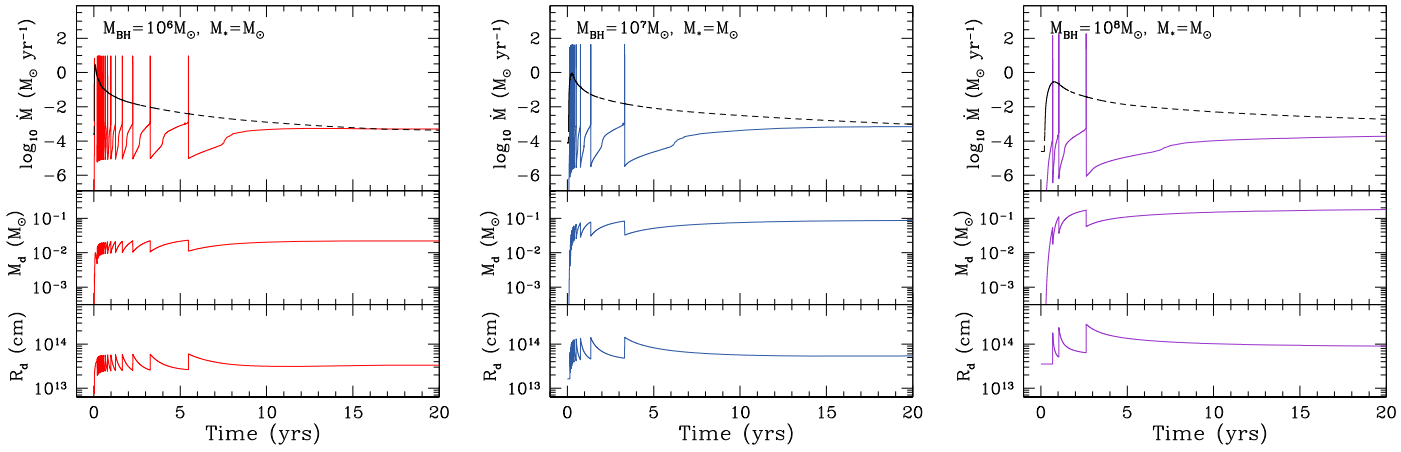

Figure 8. The same models as in Figure 7 but plotted over 20 yr instead.

fallback stream is important (as discussed in Section 2.4). For all these reasons, we are hesitant to too strongly interpret this early evolution without using a starting point that is more closely set by detailed simulations. Nevertheless, these early uncertainties do not impact the flaring activity that is exhibited later on, which is insensitive to the initial conditions.

Figure 8 shows the same models as in Figure 7, but now on a timescale of 20 yr, to highlight the longer-term evolution. We see that the waiting time between high states increases with time. This is due to the lower fallback accretion rates, which cause the disk to cycle more slowly between low and high states. The fallback rate continues to drop but is still high enough to power outburst cycles out to almost a decade.

4.2. Mass Ejections During the High State

The high states of these models all exceed the Eddington accretion rate, Equation (20), thus there is probably heavy mass loss during these phases (e.g., R. D. Blandford & M. C. Begelman 1999; L. Dai et al. 2018; L. L. Thomsen et al. 2022). In Figure 9, we plot the duration of the high states in the upper panel and an estimate of the mass lost, which is the integral

$$M_{\rm flare} = \int \dot{M}_{\rm out}(t)\,dt, \tag{21}$$

using Equation (10). This shows that, in principle, the high-state flares can occur out to $\lesssim$6 yr after the TDE. The typical

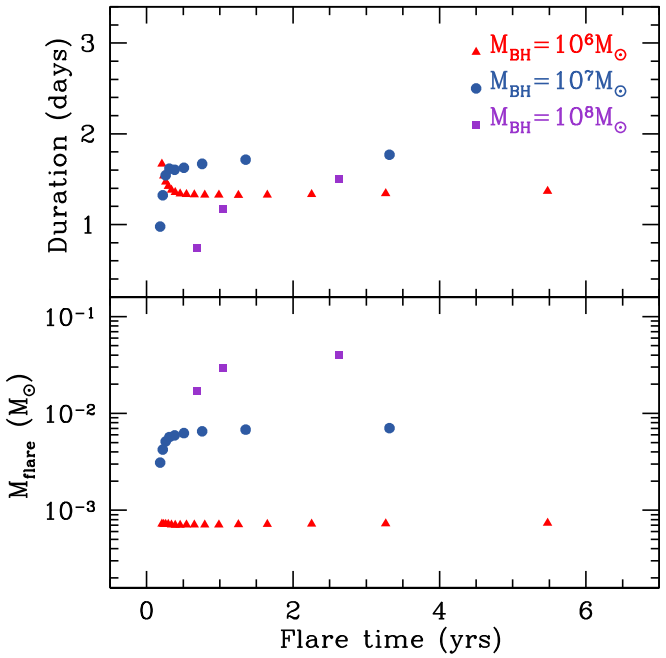

Figure 9. The duration of the high state (top panel) and estimate of the mass ejected in a flare (bottom panel) using the models from Figures 7 and 8. Different-mass BHs are designated by different symbols and colors, as indicated.

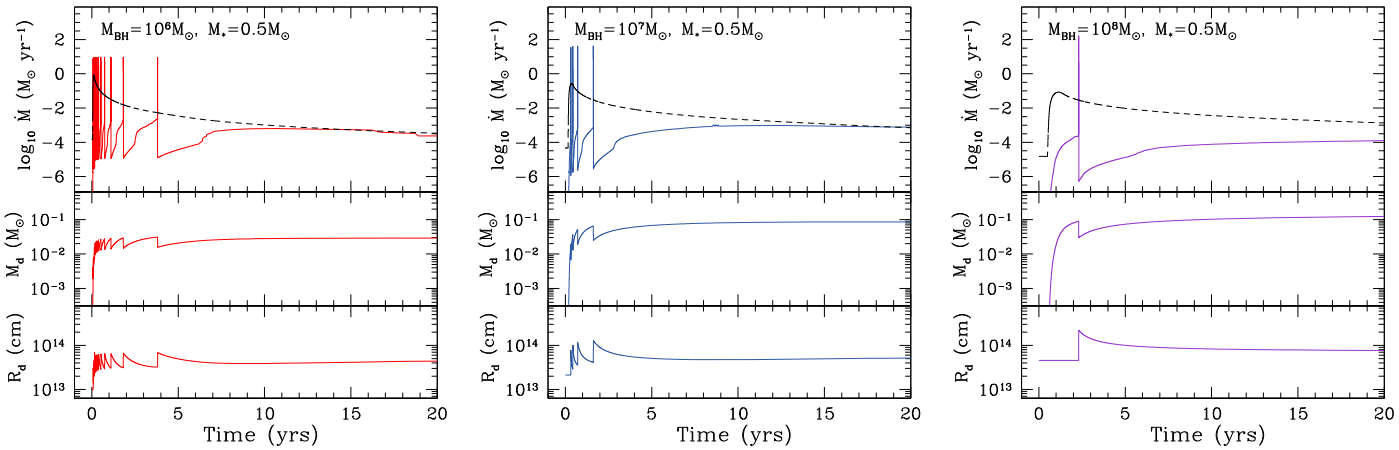

Figure 10. The same as Figure 8 but using $M_* = 0.5\,M_\odot$ and $\beta = 0.9$ instead.

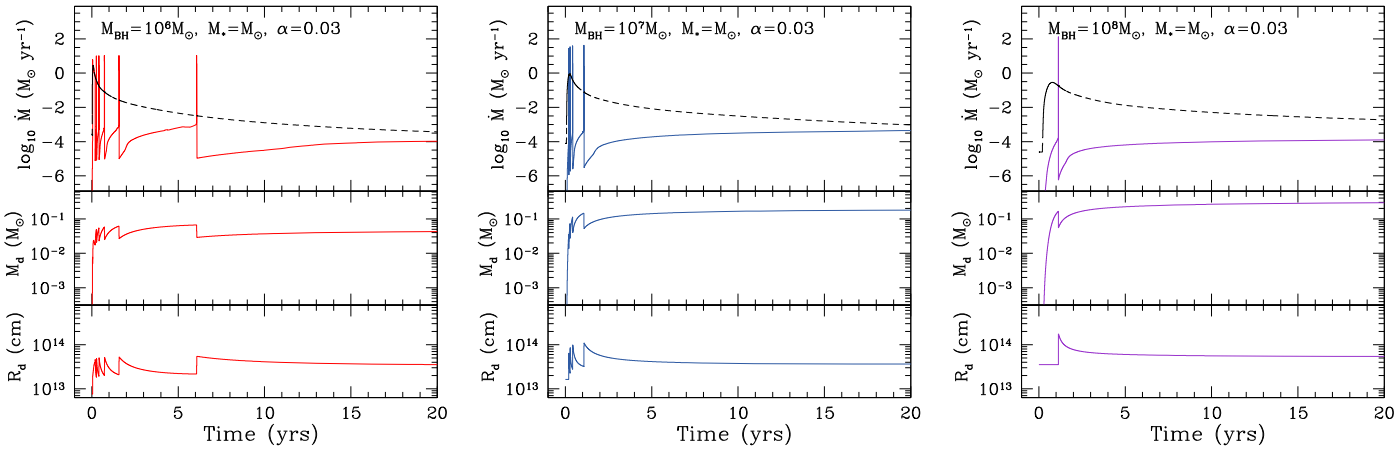

Figure 11. The same as Figure 8 but using $\alpha = 0.03$ instead.

duration is ∼1–2 days, which is fairly insensitive to the BH mass. The mass ejected during this phase $M_{\rm flare} \sim 10^{-3} - 10^{-1}\,M_\odot$, with larger BHs ejecting more mass per flare.

4.3. Changes with M_*, α, and p

In Figure 10, we explore how the time-dependent evolution changes for a lower-mass star in the TDE. We set $M_* = 0.5\,M_\odot$ and use the fallback rate for an $n = 5/3$ polytrope, since it is more appropriate for a main-sequence star of this mass. We also set $\beta = 0.9$, since this is β_c for a less centrally concentrated star. Overall, the evolution between the high and low states is slower, with less high states. The general $\dot{M}$, M_d, and R_d values are actually not that different between $M_* = M_\odot$ and $M_* = 0.5\,M_\odot$, because the fallback rates are not really that different after the peak (as highlighted by Figure 1).

In Figure 11, we rerun the simulations with $\alpha = 0.03$, corresponding to a lower disk viscosity. Again, this causes the cycling between high and low states to be slower, with many fewer high states. The actual values of $\dot{M}$, M_d, and R_d do not change that dramatically in the low state between $\alpha = 0.1$ and $\alpha = 0.03$, because these are mostly set by the physics at the transitions between states. This provides some robustness to these models, in the sense that these outbursts should happen even if we are not able to predict the exact times when the outbursts will occur.

Finally, in Figure 12, we rerun the simulations with $p = 0.2$, corresponding to less mass loss in the high state. The main impact is that the disk grows to larger sizes, due to the decreased loss of angular momentum. This in turn increases the viscous time, so that the disk evolves through less outburst cycles.

5. Comparisons to Observations

As discussed in Section 1, some of the evidence for long-lasting accretion comes in the form of late-time optical/UV emission and delayed radio flares. We thus compare our disk models with these observations here.

5.1. Late-time UV Emission

Assuming the disk radiates as a series of blackbodies at each annulus, the effective temperature at a radius r is

$$T_{\rm eff}(r) = \left\{\frac{3GM_{\rm BH}\dot{M}}{8\pi\sigma_{\rm SB}r^3}\left[1 - \left(\frac{R_i}{r}\right)\right]^{1/2}\right\}^{1/4}, \quad (22)$$

where $\sigma_{\rm SB}$ is the Stefan–Boltzmann constant. Radiative transfer effects can complicate the relationship between the observed temperature and $T_{\rm eff}$ (e.g., C. Done et al. 2012), but since we are only doing simply comparisons at this point, we save these details for future work. Since we are considering BH masses up to $10^8\,M_\odot$, the BH spin must be fairly high to allow the TDE to

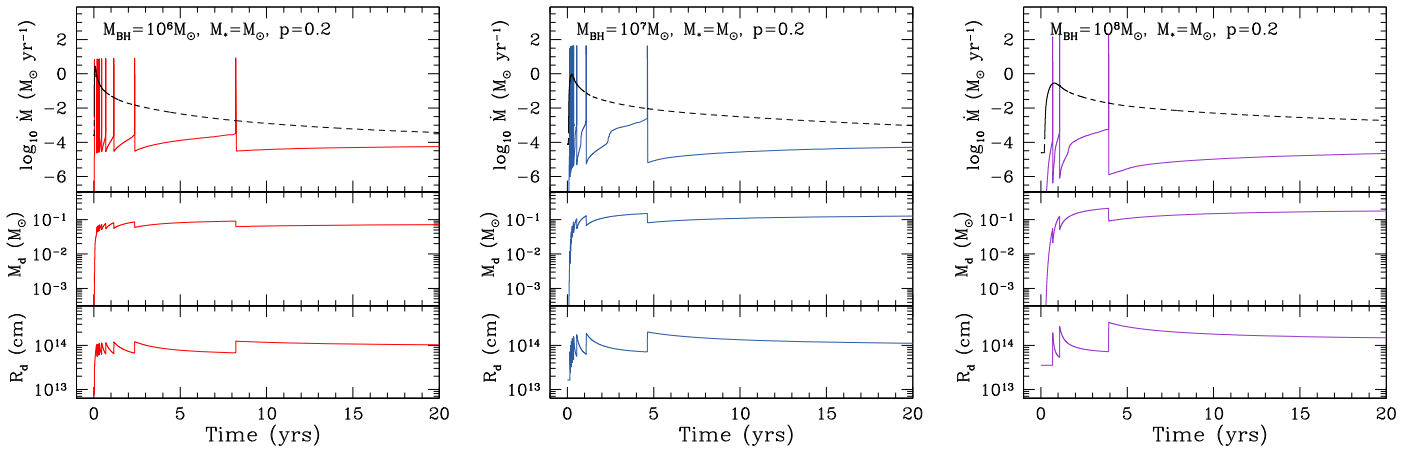

Figure 12. The same as Figure 8 but using $p = 0.2$ instead.

occur. To be consistent, we assume $R_i = R_s/2$ (a maximally spinning BH) for our spectral models. Thus, there could be strong differences between what we predict and reality at the shortest wavelengths, depending on the BH spin.

Integrating a Planck function over the entire disk gives the observed flux at a given frequency ν at a distance D (J. Frank et al. 2002):

$$F_\nu = \frac{4\pi h\nu^3 \cos\theta}{c^2 D^2} \int_{R_s}^{R_d} \frac{rdr}{\exp[h\nu/k_B T_{\rm eff}(r)] - 1}, \quad (23)$$

where θ is the inclination ($\cos\theta = 1$ for a face-on disk). The total luminosity from a disk at a given frequency is calculated by integrating the disk emission over a sphere at radius D:

$$L_\nu = 2\int_0^{2\pi}\int_0^{\pi/2} D^2 F_\nu \sin\theta d\theta d\phi, \quad (24)$$

where the factor of 2 is for the two sides of the disk. Comparing Equation (23) with the result from integrating Equation (24), we conclude that the conversion between the observed flux and the total luminosity of a disk is

$$L_\nu = \frac{2\pi D^2}{\cos\theta} F_\nu. \quad (25)$$

In contrast, an observer calculating the luminosity from an observed flux would typically not take into account the disk's emission pattern and instead simply calculate an isotropic equivalent:

$$L_\nu^{\rm iso} = 4\pi D^2 F_\nu. \quad (26)$$

So, for comparisons with observations, we proceed in the same way.

In Figure 13, we consider the range of spectral energy distributions expected for three different BH masses. In each case, we use the parameters from the calculations in Figures 7 and 8 ($M_* = M_\odot$, $\beta = 1.85$, and $\alpha = 0.1$). We assume the viewing angle is face on, so $\cos\theta = 1$. The shaded regions represent the range of accretion rates each BH exhibits while in the low state. For $M_{\rm BH} = 10^6 M_\odot$, this is 9.1×10^{-6}–$1.5 \times 10^{-3} M_\odot\,{\rm yr}^{-1}$; for $M_{\rm BH} = 10^7 M_\odot$, this is 3.4×10^{-6}–$1.0 \times 10^{-3} M_\odot\,{\rm yr}^{-1}$; and for $M_{\rm BH} = 10^8 M_\odot$, this is 8.8×10^{-7}–$5.8 \times 10^{-4} M_\odot\,{\rm yr}^{-1}$. The radius varies as well for each accretion rate, but by no more than about a factor of ~3 for a given BH mass. This shows how the overall disk emission

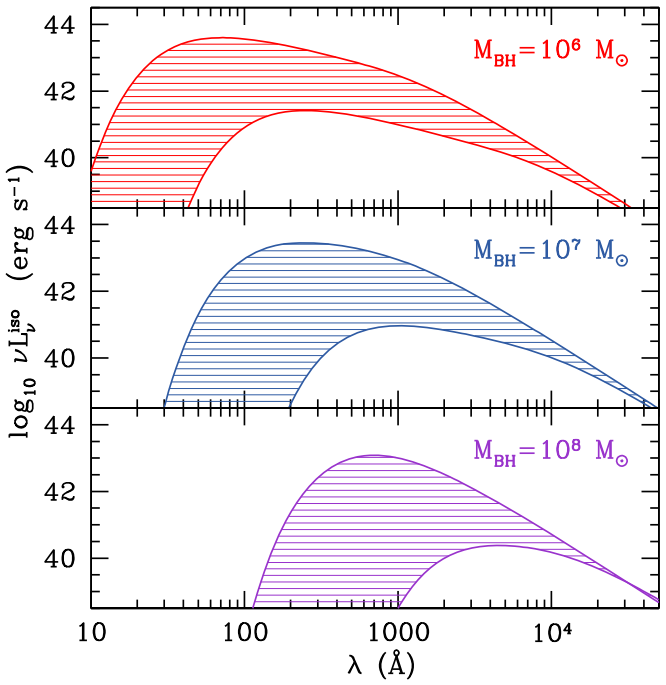

Figure 13. Characteristic spectral energy distributions for three different BH masses. In each case, the shaded region represents the range of $\dot{M}$ values possible during the low state (see the text for the specific values considered). All models use $M_* = M_\odot$, $\beta = 1.85$, $\alpha = 0.1$, $p = 0.5$, and $\cos\theta = 1$.

can vary dramatically throughout the low state and how a larger BH mass shifts the distribution to longer wavelengths.

In Figure 14, we compare the time evolutions of models with three different BH masses to the UV observations summarized in S. van Velzen et al. (2019). The models again all use $M_* = M_\odot$, $\beta = 1.85$, $\alpha = 0.1$, and a viewing angle of $\cos\theta = 1$. The filled squares are UV detections of 10 different TDEs at 295–3332 days after the maximum early emission, although we caution that for the first couple of points (at 295 and 557 days), there may be significant contribution from a nondisk source, such as a reprocessing region in the TDE. We also plot two upper limits as open triangles. Since this involves combining data from different events, these should not be viewed as a light curve but rather as just providing a range of possible luminosities and timescales. We omit plotting the luminosity when the disk is in the high state, because the super-Eddington rates may obscure the disk or at least change the

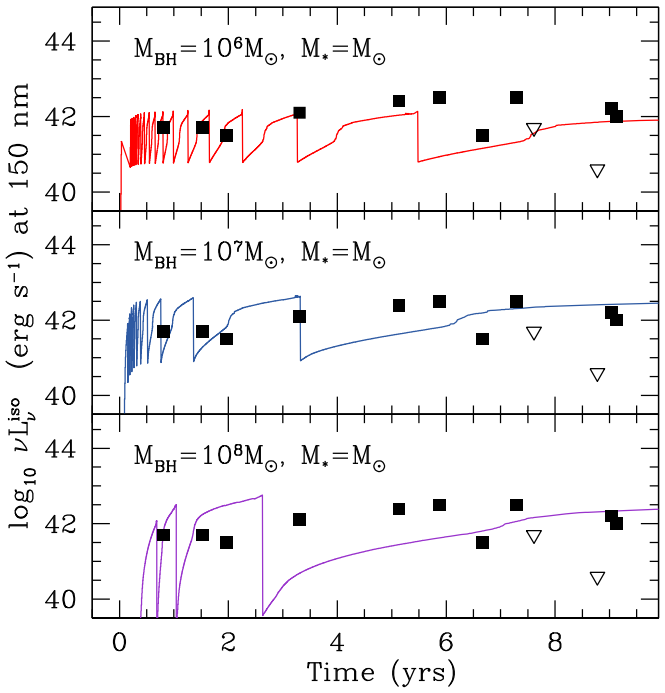

Figure 14. Comparison of the isotropic equivalent luminosity at 150 nm for three different BH masses with the observations summarized in S. van Velzen et al. (2019). Detections are shown as filled squares, while upper limits are shown as open triangles. Note that this is a combination of observations from 12 different events and should not be viewed as a light curve (this is further discussed in the text). All models use $M_* = M_\odot$, $\beta = 1.85$, $\alpha = 0.1$, $p = 0.5$, and $\cos\theta = 1$.

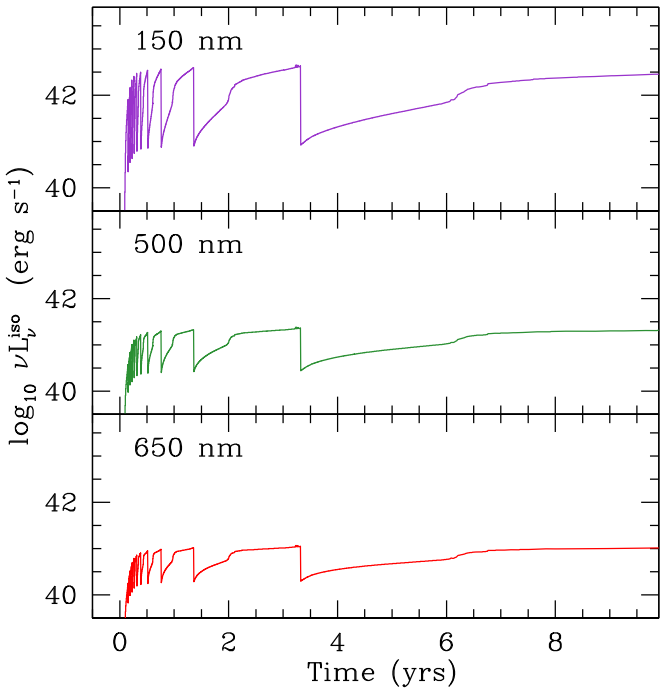

Figure 15. Comparison of how a disk light curve may appear in different wave bands using our $M_{BH} = 10^7\,M_\odot$ model (the middle panel from Figure 14). The wavelength of the emission is noted in each panel. This demonstrates that the flux variations decrease with longer wavelengths.

disk spectral energy distribution and, anyway, these last for a very short time (∼2 days) compared to the overall evolution.

This comparison shows that these models can in principle produce sufficient UV luminosity to explain the observed UV emission. One can distinctly see two components during the low-state evolution, which is due to the increased opacity from the iron bump. The two upper limits are also consistent with this picture of the late-time UV for any given system possibly being dimmer by about an order of magnitude as they evolve through the low state. In the future, it will be critical to follow the evolution of TDEs in the UV at higher cadence, to better understand the duty cycle of this emission.

From Figure 13, it is apparent that the amount of variation in luminosity depends strongly on the wavelength. To better highlight this, we compare three different wave bands in Figure 15, where 500 nm roughly corresponds to g band and 650 nm roughly corresponds to r band. This shows that longer wavelengths generally show less variation. This is consistent with the ensemble of light curves presented in A. Mummery et al. (2024), showing that the higher-cadence g- and r-band light curves generally show variations by a factor of ∼3 rather than being simply flat. This roughly matches the variations we see in Figure 13. M. Nicholl et al. (2024) also present late-time r-band observations of AT2019qiz. The variations appear somewhat smaller, maybe by a factor of ∼2, although there are large error bars, due to subtracting the host galaxy from the TDE light. To facilitate better comparisons at these longer wavelengths, it will be useful to build 1D models rather than the one-zone models we use here, to better follow material at the largest radii, where most of this light originates from.

5.2. Radio Flares

As described in Section 4, the super-Eddington phases of the evolution typically eject $M_{ej} \sim 10^{-3}$–$10^{-1}\,M_\odot$. The material will have a variety of velocities, roughly scaling with the escape velocity from each radius in the disk. In the outer parts of the disk, $v_{min} \sim 0.03c$, but near the ISCO, it can be $v_{max} \sim 0.3c$ or somewhat higher. Using the outflow rate given in Equation (10), this results in a density profile

$$\rho_{out}(v, t) = \frac{p\dot{M}\Delta t}{2\pi(vt)^3}\left(\frac{v_{min}}{v}\right)^{2p}, \quad (27)$$

where Δt is the timescale out of the outburst. Assuming a roughly spherical outflow, the optical depth of this material is

$$\tau(t) = \int_{v_{min}t}^{v_{max}t} \kappa\rho(v, t)d(vt) \approx \frac{p}{4\pi(p+1)}\frac{\kappa\dot{M}\Delta t}{(v_{min}t)^2}, \quad (28)$$

where we assume $v_{min} \ll v_{max}$. Setting $\tau \approx 1$, we can solve for the time when the material becomes optically thin, which is only ∼0.5 days. Thus, this material could reprocess the disk emission and contribute to the optical/UV luminosity, but such a phase may be difficult to catch because it is so short.

Another possibility is that this ejected material generates radio emission. As the ejecta continues to expand, it will interact with surrounding material with density n, sweeping up a mass comparable to its own at a Sedov–Taylor radius of

$$r_{TS} \approx \left(\frac{3M_{flare}}{4\pi n m_p}\right)^{1/3}, \quad (29)$$

where m_p is the proton mass. A typical radius would be $r_{\rm TS} \sim 10^{17}$–10^{18} cm, depending on the value of n, which may be higher in the circumnuclear environment. Thus, we would expect radio synchrotron emission on a timescale of ∼years. This is analogous to the radio flare model for neutron star mergers by E. Nakar & T. Piran (2011), and we would expect similar luminosities of $\sim 10^{38}\,{\rm erg\,s^{-1}}$ at around ∼gigahertz frequencies. Such a model, though, may have difficulty producing flares that fall off more quickly (e.g., see some of the radio light curves in K. D. Alexander et al. 2020). This could instead require collisions between successive ejections when the fast outer material of a later shell catches the slower inner material of an earlier shell. We save a detailed calculation of this process for future work.

Roughly speaking, though, when Y. Cendes et al. (2024) fit synchrotron models to real events, they find similar parameters to what we find here. Furthermore, tracing the velocities of the radio-emitting regions back in time requires material to be ejected after the main TDE on timescales similar to when we see disk instabilities. This all suggests that the super-Eddington flares our disk models exhibit could naturally explain the observed radio flares, which we will explore in future work. Since the amount of mass in the ejecta depends on $M_{\rm BH}$, modeling the flares could provide a complementary way to constrain the BHs in TDEs.

6. Discussion and Conclusions

We have explored the evolution of TDE accretion disks on long timescales after the initial stellar destruction. Using a semi-analytic one-zone model, we have shown that these disks naturally go into a flaring state due to a thermal instability and continued feeding by fallback accretion. The high-super-Eddington state can last for a couple of days, ejecting $\sim 10^{-3}$–$10^{-1}\,M_\odot$ of material at speeds of ∼0.03–0.3c, potentially producing radio flares that can occur up to a decade after the main TDE (e.g., Y. Cendes et al. 2024). This is interspersed with low states, where the disk luminosity rises for months to years as it grows in mass. This low state matches the late-time UV luminosities seen years after some TDEs (e.g., S. van Velzen et al. 2019). The UV luminosity can vary by over an order of magnitude in the low state, so we may only be observing events at times when the disks are especially massive and bright. This is difficult to assess, because current UV observations are fairly sparse. We find that the luminosity in the optical bands varies less, similar to the variations of a factor of ∼3 seen in the late-time r- and g-band observations (A. Mummery et al. 2024).

This work suggests there may be interesting connections between the disk state and the occurrence of radio flares. Continued monitoring in the optical/UV to characterize the disk and in the radio to follow the flares could be used to better constrain the time-dependent accretion state (e.g., A. J. Goodwin et al. 2025). We demonstrate how the rate of flare events is related to the properties of the TDE, so in the future, this may be used as another way to measure the BH mass. Although our preliminary work in Section 2.4 on the impact of fallback heating shows this could prevent flaring at early times, this should be explored in more detail in future studies.

Our $M_{\rm BH} = 10^6\,M_\odot$ disk model transitions from the high state to the low state for the first time at ∼100 days, depending on the details of the parameters chosen (e.g., see Figure 7). In contrast, the TDE AT2018fyk shows a sudden drop in X-ray emission at ∼320 and ∼500 days (T. Wevers et al. 2019, 2023), while AT2021ehb shows a similar drop at ∼320 days (Y. Yao et al. 2022). This could potentially be matched by more massive BHs. Alternatively, W. Lu (2022) speculates that these longer timescales could be easier to explain if the disk experiences an outside-in transition to a low accretion state. This process is estimated to roughly take ∼1 yr (set by when the inner disk reaches the Eddington limit), which is in better agreement with AT2018fyk and AT2021ehb. Addressing whether this occurs would require a 1D treatment rather than the one-zone model we employ here. While this is outside the scope of this work, such a calculation could be fruitful for better understanding these observations. Another complication that we do not include is the impact of magnetic fields, which can help to stabilize the TDE disks (e.g., Y. Alush & N. C. Stone 2025). Higher-cadence observations, especially in the UV, with missions like ULTRASAT (Y. Shvartzvald et al. 2024), would be helpful for constraining whether such physical effects are needed.

Our models also provide the disk properties that are present for QPEs in the star–disk collision picture. As the disk grows in the low state over many months to years, it would also presumably change the properties of the QPEs as well (duration and energy, etc). This could provide another probe of the disk physics. There could also be an additional mass source for the disk from material ablated from the QPE-producing star, and in fact I. Linial & B. D. Metzger (2024) argue that heating from the star–disk collision could help stabilize the high and low states we explore here (similar to the fallback heating we explore). This suggests that the radio flaring and optical/UV disk emission could be impacted by QPEs, providing yet another reason to conduct long-term multiwavelength monitoring of TDEs.

Acknowledgments

We thank Xiaoshan Huang, Daichi Tsuna, and Wenbin Lu for helpful discussions and feedback. We also thank the referee for useful comments and suggestions.

Appendix
Solving for the Disk Evolution

To follow the time evolution of the disk, Equations (11) and (12) are solved forward in time, using explicit time stepping. The accretion rate can vary by orders of magnitude during its evolution, so the time steps must be similarly flexible. This is done by setting the ith time step as

$$\Delta t_i = \epsilon \frac{M_d(t_{i-1})}{|\dot{M}_{\rm fb}(t_{i-1}) - \dot{M}(t_{i-1})|}, \tag{A1}$$

where ϵ is a small number that adjusts the size of the time steps, and all the parameters on the right-hand side of Equation (A1) are evaluated at the previous time step. We find good convergence for $\epsilon < 10^{-3}$.

The main challenge when finding the evolution is solving for the accretion rate $\dot{M}$. This is done using the following strategy.

1. The surface density is solved for using M_d and R_d from the previous time step and $\Sigma = M_d/(\pi R_d^2)$.
2. The temperature T is then found by numerically solving the energy balance (Equation (17)). This is done using

bisection around a temperature interval set from the temperature found in the previous time step, $T(t_{i-1})$, since for some values of Σ, there may be multiple solutions for T.

3. An important step when solving the energy equation is that for a given Σ and guess for T, the isothermal sound speed can be solved with a quadratic equation: $c_s^2 - aT^4/(3\Sigma\Omega)c_s - k_B T/(\mu m_p) = 0$.
4. Once Σ and T are found, we set $\dot{M} = 3\pi\alpha c_s^2\Sigma/\Omega$.

At this point, we solve for Δt_i using Equation (A1), then we evolve forward one time step using

$$M_d(t_i) = M_d(t_{i-1}) + \dot{M}_{\rm fb}(t_{i-1})\Delta t_i - \dot{M}(t_{i-1})\Delta t_i \quad \text{(A2)}$$

and

$$J_d(t_i) = J_d(t_{i-1}) + j_{\rm fb}\dot{M}_{\rm fb}(t_{i-1})\Delta t_i - C(GM_{\rm BH}R_d)^{1/2}\dot{M}(t_{i-1})\Delta t_i. \quad \text{(A3)}$$

The new radius is then set by using $R_d = (J_d/M_d)^2/(GM_{\rm BH})$. We then go back to the first bullet point above to start working on the next time step. Implicit in our approach is that the thermal time of the disk is always much shorter than the viscous time, so that the energy balance is always maintained. This prevents us from being forced to explicitly time evolve the internal energy of the disk. Our comparisons in Section 3 demonstrate that this assumption results in solutions that match previous work.

ORCID iDs

Anthony L. Piro https://orcid.org/0000-0001-6806-0673
Brenna Mockler https://orcid.org/0000-0001-6350-8168

References

Alexander, K. D., Berger, E., Guillochon, J., Zauderer, B. A., & Williams, P. K. G. 2016, ApJL, 819, L25
Alexander, K. D., van Velzen, S., Horesh, A., & Zauderer, B. A. 2020, SSRv, 216, 81
Alush, Y., & Stone, N. C. 2025, arXiv:2503.03811
Anumarlapudi, A., Dobie, D., Kaplan, D. L., et al. 2024, ApJ, 974, 241
Arcodia, R., Liu, Z., Merloni, A., et al. 2024, A&A, 684, A64
Arcodia, R., Merloni, A., Nandra, K., et al. 2021, Natur, 592, 704
Arcodia, R., Miniutti, G., Ponti, G., et al. 2022, A&A, 662, A49
Barniol Duran, R., Nakar, E., & Piran, T. 2013, ApJ, 772, 78
Begelman, M. C. 1979, MNRAS, 187, 237
Begelman, M. C., & Pringle, J. E. 2007, MNRAS, 375, 1070
Blandford, R. D., & Begelman, M. C. 1999, MNRAS, 303, L1
Bonnerot, C., Lu, W., & Hopkins, P. F. 2021, MNRAS, 504, 4885
Bricman, K., & Gomboc, A. 2020, ApJ, 890, 73
Cannizzo, J. K., Lee, H. M., & Goodman, J. 1990, ApJ, 351, 38
Cendes, Y., Berger, E., Alexander, K. D., et al. 2022, ApJ, 938, 28
Cendes, Y., Berger, E., Alexander, K. D., et al. 2024, ApJ, 971, 185
Chakraborty, J., Kara, E., Masterson, M., et al. 2021, ApJL, 921, L40
Chevalier, R. A. 1998, ApJ, 499, 810
Christy, C. T., Alexander, K. D., Margutti, R., et al. 2024, ApJ, 974, 18
Dai, L., Escala, A., & Coppi, P. 2013, ApJL, 775, L9
Dai, L., McKinney, J. C., Roth, N., Ramirez-Ruiz, E., & Miller, M. C. 2018, ApJL, 859, L20
Done, C., Davis, S. W., Jin, C., Blaes, O., & Ward, M. 2012, MNRAS, 420, 1848
Franchini, A., Bonetti, M., Lupi, A., et al. 2023, A&A, 675, A100
Frank, J., King, A., & Raine, D. J. 2002, Accretion Power in Astrophysics (3rd ed.; Cambridge: Cambridge Univ. Press)
Gafton, E., & Rosswog, S. 2019, MNRAS, 487, 4790
Giustini, M., Miniutti, G., & Saxton, R. D. 2020, A&A, 636, L2
Goodwin, A. J., Alexander, K. D., Miller-Jones, J. C. A., et al. 2023b, MNRAS, 522, 5084
Goodwin, A. J., Miller-Jones, J. C. A., van Velzen, S., et al. 2023a, MNRAS, 518, 847
Goodwin, A. J., Mummery, A., Laskar, T., et al. 2025, ApJ, 981, 122
Guillochon, J., & Ramirez-Ruiz, E. 2013, ApJ, 767, 25
Guillochon, J., & Ramirez-Ruiz, E. 2015, ApJ, 809, 166
Hirose, S., Krolik, J. H., & Blaes, O. 2009, ApJ, 691, 16
Horesh, A., Cenko, S. B., & Arcavi, I. 2021a, NatAs, 5, 491
Horesh, A., Sfaradi, I., Fender, R., et al. 2021b, ApJL, 920, L5
Hu, H., Inayoshi, K., Haiman, Z., Quataert, E., & Kuiper, R. 2022, ApJ, 934, 132
Iglesias, C. A., & Rogers, F. J. 1996, ApJ, 464, 943
Jankovifç, T., Bonnerot, C., & Gomboc, A. 2024, MNRAS, 529, 673
Jiang, Y. F., Davis, S. W., & Stone, J. M. 2016, ApJ, 827, 10
Jiang, Y.-F., Stone, J. M., & Davis, S. W. 2013, ApJ, 778, 65
Kumar, P., Narayan, R., & Johnson, J. L. 2008, MNRAS, 388, 1729
Kaur, K., Stone, N. C., & Gilbaum, S. 2023, MNRAS, 524, 1269
Law-Smith, J. A. P., Coulter, D. A., Guillochon, J., Mockler, B., & Ramirez-Ruiz, E. 2020, ApJ, 905, 141
Levan, A. J., Tanvir, N. R., Cenko, S. B., et al. 2011, Sci, 333, 199
Lightman, A. P., & Eardley, D. M. 1974, ApJL, 187, L1
Linial, I., & Metzger, B. D. 2023, ApJ, 957, 34
Linial, I., & Metzger, B. D. 2024, ApJ, 973, 101
Lu, W. 2022, in Handbook of X-ray and Gamma-Ray Astrophysics, ed. C. Bambi & A. Sangangelo (Singapore: Springer), 3
Lu, W., Matsumoto, T., & Matzner, C. D. 2024, MNRAS, 533, 979
MacLeod, M., Guillochon, J., & Ramirez-Ruiz, E. 2012, ApJ, 757, 134
Matsumoto, T., & Piran, T. 2024, ApJ, 971, 49
Metzger, B. D., Piro, A. L., & Quataert, E. 2008, MNRAS, 390, 781
Miniutti, G., Giustini, M., Arcodia, R., et al. 2023a, A&A, 674, L1
Miniutti, G., Giustini, M., Arcodia, R., et al. 2023b, A&A, 670, A93
Miniutti, G., Saxton, R. D., Giustini, M., et al. 2019, Natur, 573, 381
Mishra, B., Fragile, P. C., Johnson, L. C., & Kluźniak, W. 2016, MNRAS, 463, 3437
Mockler, B., Guillochon, J., & Ramirez-Ruiz, E. 2019, ApJ, 872, 151
Mou, G., Wang, T., Wang, W., & Yang, J. 2022, MNRAS, 510, 3650
Mummery, A., & Balbus, S. A. 2020, MNRAS, 492, 5655
Mummery, A., van Velzen, S., Nathan, E., et al. 2024, MNRAS, 527, 2452
Nakar, E., & Piran, T. 2011, Natur, 478, 82
Nicholl, M., Pasham, D. R., Mummery, A., et al. 2024, Natur, 634, 804
Oda, H., Machida, M., Nakamura, K. E., & Matsumoto, R. 2009, ApJ, 697, 16
Pan, X., Li, S.-L., Cao, X., Miniutti, G., & Gu, M. 2022, ApJL, 928, L18
Phinney, E. S. 1989, in IAU Symp. 136, The Center of the Galaxy, ed. M. Morris (Cambridge: Cambridge Univ. Press), 543
Quintin, E., Webb, N. A., Guillot, S., et al. 2023, A&A, 675, A152
Rees, M. J. 1988, Natur, 333, 523
Ryu, T., Krolik, J., Piran, T., & Noble, S. C. 2020, ApJ, 904, 98
Sadowski, A. 2016, MNRAS, 459, 4397
Sakimoto, P. J., & Coroniti, F. V. 1981, ApJ, 247, 19
Sfaradi, I., Beniamini, P., Horesh, A., et al. 2024, MNRAS, 527, 7672
Sfaradi, I., Horesh, A., Fender, R., et al. 2022, ApJ, 933, 176
Shakura, N. I., & Sunyaev, R. A. 1973, A&A, 24, 337
Shakura, N. I., & Sunyaev, R. A. 1976, MNRAS, 175, 613
Shen, R.-F., & Matzner, C. D. 2014, ApJ, 784, 87
Shvartzvald, Y., Waxman, E., Gal-Yam, A., et al. 2024, ApJ, 964, 74
Steinberg, E., & Stone, N. C. 2024, Natur, 625, 463
Stone, J. M., & Pringle, J. E. 2001, MNRAS, 322, 461
Stone, N., Sari, R., & Loeb, A. 2013, MNRAS, 435, 1809
Teboul, O., & Metzger, B. D. 2023, ApJL, 957, L9
Thomsen, L. L., Kwan, T. M., Dai, L., et al. 2022, ApJL, 937, L28
van Velzen, S., Stone, N. C., Metzger, B. D., et al. 2019, ApJ, 878, 82
Warner, B. 1995, Cataclysmic Variable Stars (Cambridge: Cambridge Univ. Press)
Watarai, K.-y. 2006, ApJ, 648, 523
Wevers, T., Coughlin, E. R., Pasham, D. R., et al. 2023, ApJL, 942, L33
Wevers, T., Pasham, D. R., Jalan, P., Rakshit, S., & Arcodia, R. 2022, A&A, 659, L2
Wevers, T., Pasham, D. R., van Velzen, S., et al. 2019, MNRAS, 488, 4816
Yao, Y., Lu, W., Guolo, M., et al. 2022, ApJ, 937, 8
Yuan, F., & Narayan, R. 2014, ARA&A, 52, 529
Zauderer, B. A., Berger, E., Margutti, R., et al. 2013, ApJ, 767, 152
Zhuang, J., Shen, R.-F., Mou, G., & Lu, W. 2025, ApJ, 979, 109